

# Journal of Biomedical Optics

BiomedicalOptics.SPIEDigitalLibrary.org

## **Volumetric imaging of rod and cone photoreceptor structure with a combined adaptive optics-optical coherence tomography-scanning laser ophthalmoscope**

Elaine M. Wells-Gray  
Stacey S. Choi  
Robert J. Zawadzki  
Susanna C. Finn  
Cherry Greiner  
John S. Werner  
Nathan Doble

**SPIE.**

Elaine M. Wells-Gray, Stacey S. Choi, Robert J. Zawadzki, Susanna C. Finn, Cherry Greiner, John S. Werner, Nathan Doble, "Volumetric imaging of rod and cone photoreceptor structure with a combined adaptive optics-optical coherence tomography-scanning laser ophthalmoscope," *J. Biomed. Opt.* 23(3), 036003 (2018), doi: 10.1117/1.JBO.23.3.036003.

# Volumetric imaging of rod and cone photoreceptor structure with a combined adaptive optics-optical coherence tomography-scanning laser ophthalmoscope

Elaine M. Wells-Gray,<sup>a,\*</sup> Stacey S. Choi,<sup>a,b</sup> Robert J. Zawadzki,<sup>c</sup> Susanna C. Finn,<sup>d</sup> Cherry Greiner,<sup>e</sup> John S. Werner,<sup>c</sup> and Nathan Doble<sup>a,b</sup>

<sup>a</sup>The Ohio State University, College of Optometry, Columbus, Ohio, United States

<sup>b</sup>The Ohio State University, Department of Ophthalmology and Vision Science, Havener Eye Institute, Columbus, Ohio, United States

<sup>c</sup>University of California Davis, Vision Science and Advanced Retinal Imaging Laboratory, UC Davis Eye Center, Sacramento, California, United States

<sup>d</sup>University of Massachusetts Lowell, Lowell Center for Space Science and Technology, Lowell, Massachusetts, United States

<sup>e</sup>InfraredX, Burlington, Massachusetts, United States

**Abstract.** We have designed and implemented a dual-mode adaptive optics (AO) imaging system that combines spectral domain optical coherence tomography (OCT) and scanning laser ophthalmoscopy (SLO) for *in vivo* imaging of the human retina. The system simultaneously acquires SLO frames and OCT B-scans at 60 Hz with an OCT volume acquisition time of 4.2 s. Transverse eye motion measured from the SLO is used to register the OCT B-scans to generate three-dimensional (3-D) volumes. Key optical design considerations include: minimizing system aberrations through the use of off-axis relay telescopes, conjugate pupil plane requirements, and the use of dichroic beam splitters to separate and recombine the OCT and SLO beams around the nonshared horizontal scanning mirrors. To demonstrate system performance, AO-OCT-SLO images and measurements are taken from three normal human subjects ranging in retinal eccentricity from the fovea out to 15-deg temporal and 20-deg superior. Also presented are *en face* OCT projections generated from the registered 3-D volumes. The ability to acquire high-resolution 3-D images of the human retina in the midperiphery and beyond has clinical importance in diseases, such as retinitis pigmentosa and cone-rod dystrophy. © 2018 Society of Photo-Optical Instrumentation Engineers (SPIE) [DOI: 10.1117/1.JBO.23.3.036003]

Keywords: adaptive optics; optical coherence tomography; scanning laser ophthalmoscopy; photoreceptors; cones; rods; 3-D imaging.

Paper 170701R received Oct. 30, 2017; accepted for publication Jan. 29, 2018; published online Mar. 5, 2018.

## 1 Introduction

The use of adaptive optics (AO) to overcome aberrations in the eye enables *in vivo* cellular-level imaging of the human retina. Since its first use in a flood-illuminated fundus camera,<sup>1</sup> AO has been successfully applied to both scanning laser ophthalmoscopy (SLO)<sup>2</sup> and optical coherence tomography (OCT),<sup>3–6</sup> providing insight into retinal microstructure in both healthy and diseased eyes. In addition to fundamental differences in their image formation, SLO and OCT provide complementary views of the retina, *en face* and typically cross sectional, respectively. OCT allows mapping of blood perfusion by OCT angiography but can only detect backscattered light, making SLO the preferred modality for detection of intrinsic and extrinsic fluorescence. Combining these two techniques into a single multimodal imaging platform allows examination of retinal microstructure in more detail than provided by either modality alone.

Several research groups have pursued a dual OCT-SLO approach in the development of their retinal AO imaging systems. Primary differences include the OCT configuration and

whether the system acquires the two channels simultaneously or sequentially. In 1998, prior to the application of AO in retinal imaging, Podoleanu and Jackson<sup>7</sup> reported the first combined OCT-SLO system, which utilized a time-domain (TD) transverse scanning (TS)-OCT configuration. The first AO-equipped combined OCT-SLO systems adopted a similar approach, beginning with an AO-(TS)-OCT-SLO by Merino et al.<sup>8</sup> Operating at a 2-Hz simultaneous OCT C-scan and SLO frame rate, it employed a 37-actuator membrane deformable mirror (DM) to achieve AO-corrected improvements to both sensitivity and lateral resolution. Pircher et al.<sup>9</sup> developed an AO-(TS)-OCT-SLO capable of 28-Hz simultaneous OCT (C-scan) and SLO acquisition, and with AO correction it was able to image cones within 0.5 deg from the fovea. A later generation device by the same group<sup>10</sup> achieved three-dimensional (3-D) AO-corrected resolution sufficient to visualize rods in both the *en face* SLO and OCT images at 8-deg temporal retina (TR).

Fourier-domain OCT has also been employed in combined AO imaging systems. Mujat et al.<sup>11</sup> used sequential acquisition of swept source (SS)-OCT and SLO in their multimodal clinical AO system. Combined AO-OCT-SLO systems utilizing spectral

\*Address all correspondence to: Elaine M. Wells-Gray, E-mail: [wells-gray.1@osu.edu](mailto:wells-gray.1@osu.edu)

domain (SD)-OCT include the sequential acquisition system described by Meadway et al.,<sup>12</sup> as well as systems by Zawadzki et al.<sup>13</sup> and Hammer et al.,<sup>14</sup> which both demonstrated simultaneous acquisition of the two channels. (SD)-OCT and (SS)-OCT offer faster acquisition speeds than (TD)-OCT, which is beneficial for reducing eye motion artifacts; however, scanner and timing signaling become more complicated because the two imaging beams are not identically scanned on the retina, as with the previously described AO-(TS)-OCT-SLO systems.

An advantage of simultaneous (as opposed to sequential) AO-OCT and AO-SLO acquisition is that the AO-SLO provides a rapid snapshot of the transverse (*en face*) eye motion, which can be used for 3-D volume registration. 3-D AO-OCT imaging has received considerable interest in recent years,<sup>6,15–18</sup> but eye motion remains a challenge. Two approaches for dealing with the eye motion artifacts in stand-alone AO-OCT have been the implementation of dynamic eye tracking systems<sup>10,14,19</sup> and increasing acquisition speed.<sup>16,20</sup> Using the SLO image for this purpose represents a third option. Felberer et al.<sup>10</sup> used eye motion measured with strip-based AO-SLO registration to render 3-D data from their AO-(TS)-OCT-SLO, which operated using a single wavelength and identical scanning for both channels. The system described by Zawadzki et al.<sup>13</sup> instead used two different light sources with different scanning geometries, but also used the SLO measured transverse motion to register the volumetric AO-OCT data.

Here, we describe a newly implemented AO-(SD)-OCT-SLO that employs two separate SLD light sources (SLO:  $680 \pm 3$  nm, OCT:  $860 \pm 70$  nm) and provides simultaneous OCT and SLO acquisition. Many aspects of this system are an extension of that described by Zawadzki et al.<sup>13</sup> including the scanner configuration, spectral-domain OCT detection, and the use of dichroic beam splitters (DBS) to combine and split the beams. However, the current system incorporates a newly designed, off-axis aberration-minimizing optical layout, faster volume scanning (4.2-s acquisition), and improvements in resolution. The broadband SLD OCT light source provides a theoretical axial resolution of  $1.7 \mu\text{m}$ , on par with the best resolution provided by current AO-OCT systems. Theoretical and experimental system performance are presented, first using a model eye and then with *in vivo* retinal images from three healthy human subjects. The results demonstrate the system's ability to image photoreceptors with ultrahigh resolution ( $\sim 2 \times 2 \times 2 \mu\text{m}$ ) over a wider range of retinal eccentricities than previously reported.

## 2 Methods

### 2.1 Optical Layout

Figure 1 shows the layout of the combined AO-OCT-SLO system sample arm, which utilizes both common and noncommon optical paths for the OCT and SLO channels. The OCT reference arm is not shown. The noncommon-path locations are: (i) the OCT and SLO light delivery and detection paths (dashed blue and green lines) and (ii) the separated OCT and SLO beams at the horizontal galvanometric scanner (GS1) and the horizontal resonant scanner (RS) (solid blue and green lines). The two beams are coincident throughout the rest of the optical system (solid red lines), which is designed using 12 silvered spherical mirrors (SM1 to SM12) that form six 4-*f* telescopes. The two beams are coupled and decoupled using DBS: one in the delivery/detection arm (DBS1) and one each before (DBS2)

and after (DBS3) the horizontal scanners. The system is housed on a  $3 \times 4$  ft. optical table. The main system specifications, optical components, and electronic instrumentation are given in Table 1.

#### 2.1.1 Design goals and constraints

The layout of the system was designed and optimized using Zemax optical software (Zemax LLC, Kirkland, Washington). During this process, we sought to achieve diffraction-limited resolution over a  $1 \times 2$  deg field of view (FOV) and to allow at least  $\pm 3$  diopters of defocus [approximate measurement range of the wavefront sensor (WFS)] to pass through the system without vignetting of the beam.

A key to achieving the desired resolution was minimizing the system aberrations that arise from off-axis incidence of the beams onto the spherical mirrors. The 12 spherical mirrors (SM1:SM12) were grouped into three pairs of 4-*f* telescopes, with the out-of-plane configuration of each pair (four mirrors) designed to minimize system aberrations (primarily astigmatism<sup>21–23</sup>) in both retinal and pupil planes.<sup>24</sup> The angles of incidence for each mirror in the system were first determined using the equations presented by Gómez-Vieyra et al.<sup>25</sup> and subsequently optimized using Zemax. Focal lengths of SM1:SM12 range from 200 to 1000 mm, with all angles of incidence  $< 6$  deg.

An additional design criterion was the ability to image in the midperiphery ( $> 15$  deg from the fovea) in all meridians. A 3-in. diameter pellicle beamsplitter, placed after the last flat mirror, allows a fixation target displayed on a computer monitor to be viewed by the subject. When the pellicle is centered with respect to the optical axis but rotated 45 deg, the subject can fixate out to  $\sim 12$  deg in each meridian. To allow imaging into the midperiphery in either the nasal or temporal regions of the retina, the pellicle is laterally offset (left or right) such that a fixation target can be viewed out to  $\sim 25$  deg. Similarly, the pellicle can be raised or lowered to image out to  $\sim 25$  deg in the inferior or superior meridians.

#### 2.1.2 Conjugate pupil planes

The horizontal scanners (RS and GS1), the common vertical scanner (GS2), the DM, and the WFS are positioned in conjugate pupil planes (PPs). The WFS was placed in the conjugate PP closest to the detection paths (i.e., farthest from the eye), to minimize the noncommon-path errors. The DM, with an active surface diameter of 13.5 mm, represents the PP with the largest diameter, and therefore its placement close to the eye (a 7.15-mm PP diameter) minimizes magnification changes and helps reduce system aberrations. However, placing the DM after the scanners introduces the potential for PP motion as the beam is scanned. The effect of pupil wander at the DM was investigated in Zemax, finding the maximum beam translation to be 1.1 mm ( $\sim 8\%$  of the 13.5-mm beam) for the case of a 1 deg horizontal scanning field. The vertical drift was found to be only 0.2 mm. Despite this slight drift, diffraction-limited resolution is possible over the entire imaging field.

### 2.2 Scanning Laser Ophthalmoscopy Subsystem

In the SLO delivery arm, the  $680 \pm 3$ -nm beam first passes through an acousto-optic modulator (AOM) with a 55% duty cycle that allows light to pass through to the eye only during

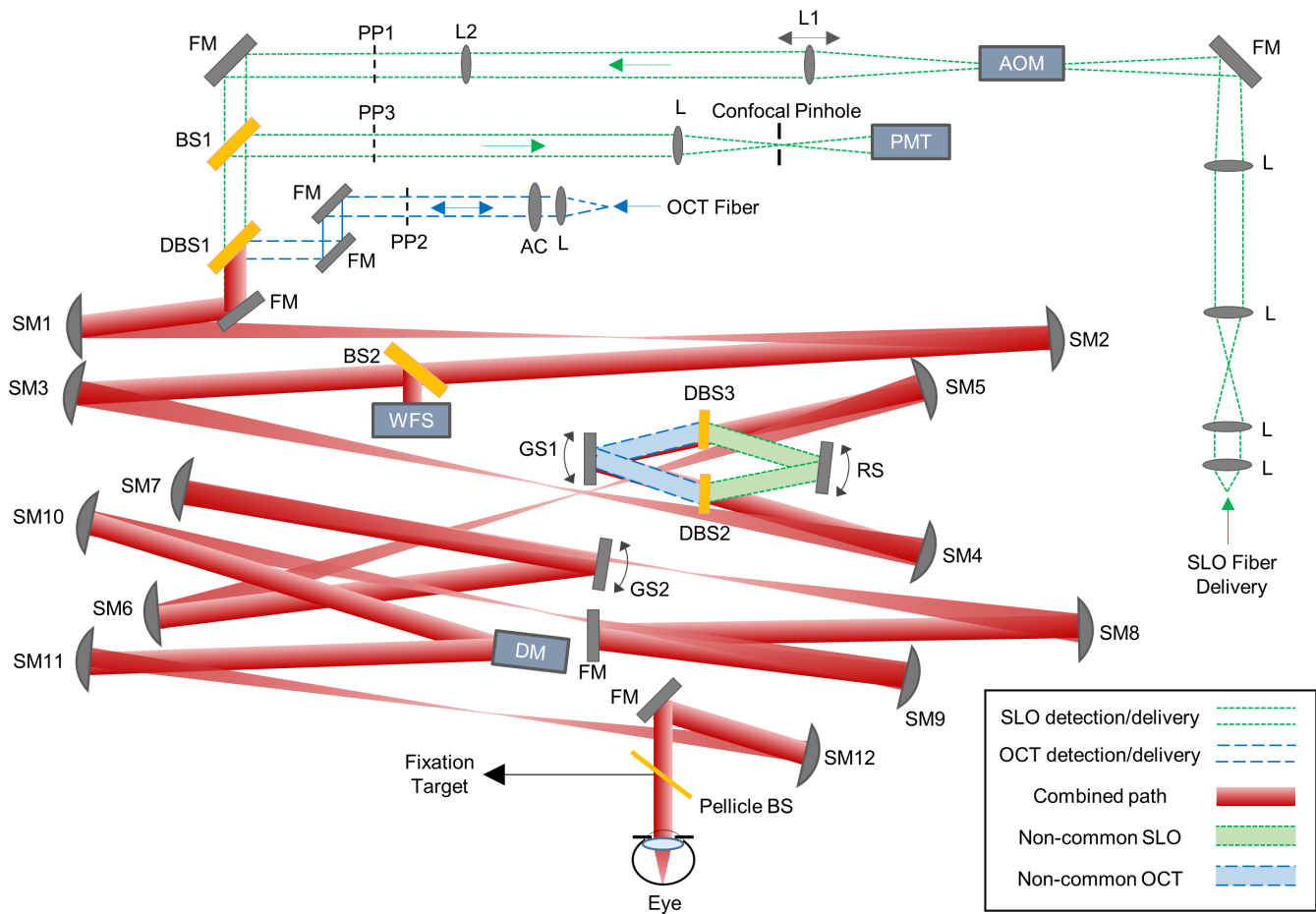


**Fig. 1** Layout of the combined AO-OCT-SLO system. The OCT reference arm is not shown. Both the SLO and OCT beams are incident into the system through single mode fibers and collimated. The OCT beam then passes through a zero power AC lens. The SLO beam is modulated by an AOM with a 55% duty cycle. SLO and OCT beam diameters are fixed by irises located in pupil conjugate planes, PP1 and PP2, respectively. The two beams are combined together at DBS1, then follow the same path through the first two spherical mirror telescopes (SM1:SM2, SM3:SM4) before being separated at DBS2. The SLO beam then travels to the RS and the OCT beam to GS1. The beams are recombined by DBS3 before propagating through the remaining telescopes (SM5:SM12) and to the eye. The vertical scanning galvo, GS2, is common to both beams, with the OCT beam being recoupled back into its delivery fiber. The SLO beam is reflected at BS1 (10:90 T:R) into its detection arm and imaged onto the PMT, mounted with a confocal pinhole. Either the OCT or SLO beam can be used to provide the signal to the WFS camera via BS2 through the use of an appropriate camera mounted filter. Abbreviations: AC, achromatizing lens; AOM, acousto-optic modulator; L, lens; FM, flat mirror; BS, beamsplitter; DBS, dichroic beamsplitter; WFS, wavefront sensor; PMT, photomultiplier tube; DM, deformable mirror; L1, translating lens; L2, chromatic aberration correction lens ( $-0.36$  diopter); PP, pupil plane; RS, resonant scanner; GS, galvo scanner; and SM, spherical mirror.

the relatively linear portion of the sinusoidal motion of the RS. This allows for imaging on both the forward and backward scans, although only the images acquired on the forward scan are generally used for image registration. The beam size is set by the aperture stop at PP1. At DBS1 (10:90 T:R), the beam is combined with the OCT. The two beams then travel coincidentally to the eye, except at the horizontal scanners (GS1 and RS), as previously mentioned. The RS scans the SLO beam in the horizontal direction at 16 kHz while GS2 scans the beam vertically at 60 Hz (see Fig. 2). Light returning from the eye is imaged onto a PMT aligned with a confocal pinhole (1 or 2 Airy disk diameters for the data presented here). To account for the longitudinal chromatic aberration between the SLO and OCT beams in the eye ( $\sim 0.36$  diopters<sup>26</sup>), L2 was introduced into the SLO delivery arm to provide an intentional

defocus between the beams. This allows both the OCT and SLO beams to be focused on the same retinal layer simultaneously. Additionally, L1 was mounted on a stage and can be translated axially for fine adjustment or to provide a desired offset between the focus of the two beams.

### 2.3 Optical Coherence Tomography Subsystem

The  $860 \pm 70$ -nm SLD OCT source is split by an 80:20 fiber coupler with 80% going to the reference arm and 20% to the sample arm. Immediately after collimation, a custom-designed achromatizing lens (AC) in the sample arm compensates for the longitudinal chromatic aberration of the eye that would otherwise arise due to the wide bandwidth of the light source.<sup>27</sup> Upon combining with the SLO beam at DBS1, the OCT

**Table 1** Primary optical components and hardware.

	Specification	Part no./manufacturer
<b>OCT channel</b>		
Light source	860 ± 70 nm SLD	BroadLighter T-860-HP, Superlum Inc., Ireland
A-scan rate	43 kHz	
A-scans per B-scan	600	
B-scans per volume	250	
Vol. Acq. time	4.2 s	
Scanner (B-scan)	60 Hz galvo (shared with SLO)	Electro-Optical Products Corporation (EOPC), Ridgewood, New York
Scanner (volume)	0.24 Hz galvo	EOPC
Spectrometer	Cobra HR (800 to 930 nm)	Wasatch Photonics, Durham, North Carolina
Diffraction grating	0.065 nm/pixel	Wasatch Photonics
Fiber coupler	80:20 splitting ratio	AC Photonics, Santa Clara, California
Camera	4096 pixels CMOS, central 2048 used, line rate = 23 μs	Sprint spL4048-140k, Basler, Ahrensburg, Germany
<b>SLO channel</b>		
Light source	680 ± 3 nm SLD	BroadLighter T-680-HP, Superlum Inc., Ireland
AOM	55% duty cycle	Crystal Technology
PMT	H7422-50	Hamamatsu Photonics, Shizuoka, Japan
PMT amplifier	HCA-40M-100K-C	Femto, Berlin, Germany
Frame rate	60 Hz	
Pixels	512 (H) × 230 (V)	
Scanner (H)	Resonant at 16 kHz	EOPC
Scanner (V/frame)	60 Hz galvo (shared with OCT)	
<b>AO</b>		
SH-WFS Beacon	OCT imaging beam (SLO can be used)	
SH-WFS lenslet array	26 × 26 lenslets, $f = 3.1$ mm	
SH-WFS camera	SHSCam AR-S-150-GE	Optocraft, Erlangen, Germany
SH-WFS diameter	3.4 mm	
Sampling frequency	25 Hz	
Closed-loop frequency	~1 to 2 Hz	
DM	DM97-15	ALPAO, Montbonnot, France
DM diameter	13.5 mm	
Control software	ALPAO CoreEngine	ALPAO
<b>Eye</b>		
Pupil diameter (eye)	7.15 mm	
FOV (retina)	Up to 1 deg × 2 deg (H × V)	

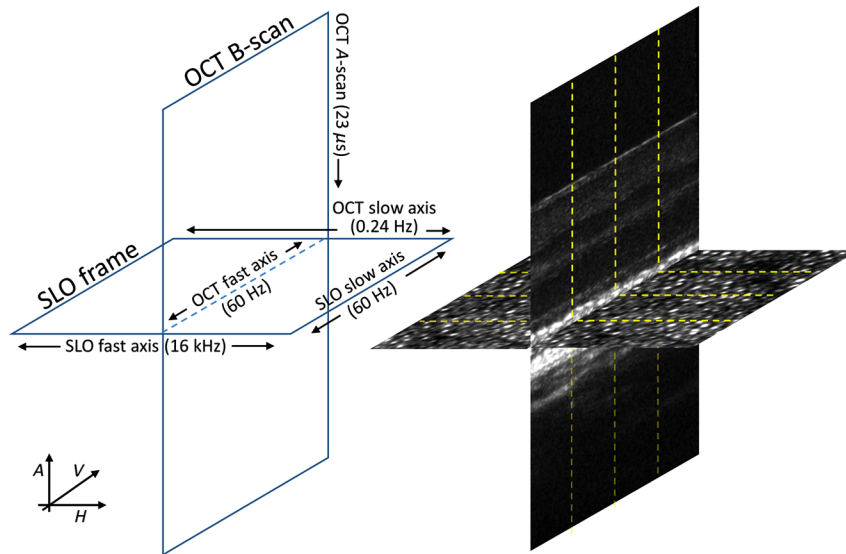


**Fig. 2** Image and scanner orientation. The vertical ( $V$ ) dimension of each image is scanned by the shared 60 Hz galvo (GS2). The SLO horizontal ( $H$ ) dimension is scanned by the 16 kHz RS, whereas the OCT  $H$  dimension is scanned by the (optional) 0.24 Hz galvo (GS1). OCT A-scan direction is denoted  $A$  (axial). The dashed yellow lines (right) indicate the orientation of strips used for AO-SLO, AO-OCT, and volume registration.

beam follows the same path through the system with the exception between DBS2 and DBS3. GS2 scans the OCT beam vertically at 60 Hz, whereas GS1 scans horizontally at 0.24 Hz and allows volume scanning. Note that GS2 is the shared vertical scanner for both the SLO and OCT and that B-scans are acquired vertically, as shown in Fig. 2. The light reflected from the eye is coupled back into the initial delivery fiber, recombined with that from the reference beam fiber, and then sent to the spectrometer—details are provided in Table 1. The reference arm (not shown in Fig. 1) is located on the main surface of the optical table, whereas the OCT sample arm (and the SLO optics) are constructed on an optical breadboard elevated 8 in above the table surface. The reference arm is constructed from elements that match the dispersion of each element in the sample arm, and includes a 2-cm-thick water-filled cuvette to match the ocular dispersion.

## 2.4 SLO-OCT Scanning, Timing, and Acquisition

A single OCT B-scan and a single SLO frame are acquired simultaneously at 60 Hz. The OCT A-scan rate is 43 kHz, with 600 A-scans per B-scan and 250 B-scans per volume. Images are acquired using two frame grabbers housed in a single host computer: a Matrox Helios XA for the SLO and Matrox Solios eV CL for the OCT (Matrox, Dorval, Quebec, Canada). Synchronization is achieved through a custom-built timing box that uses the 16 kHz RS frequency as a master clock for generating the signals that drive GS1 and GS2, trigger frame grabber acquisition, and control the AOM beam switching. The start of acquisition of the first OCT B-scan triggers the start of simultaneous acquisition of SLO frames. In line-scanning mode (i.e., GS1 off), the first and last frames are prompted by the system operator. During volume-scanning mode, coacquisition of both images starts with a trigger from the timing box generated at the start of the GS1 scan and ends upon recording 250 OCT B-scans (one volume) and SLO frames. Acquisition control and user

input are performed using executable functions written in C/C++ using the Matrox Imaging Library (MIL).

## 2.5 Adaptive Optics Subsystem

A high-speed 97-actuator DM is used in combination with a Shack–Hartmann WFS using the ALPAO Core Engine software in MATLAB (Mathworks, Natick, Massachusetts). AO control is performed by the same computer that houses the OCT and SLO frame grabber boards. Although either the SLO or OCT beam can be used to provide the signal to the AO system when the subsystems are operated independently, for combined AO-OCT-SLO operation, the OCT beam drives the loop, with the SLO light being rejected at the WFS using a high-pass wavelength filter. The DM is used to provide focal plane adjustment to scan different retinal depths.

## 2.6 Image Processing and Registration

Individual SLO frames are first dewarped to remove distortion introduced by the sinusoidal motion of the RS, then registered to remove eye motion using a strip-wise correlation approach,<sup>28</sup> and finally averaged to increase signal-to-noise. Frames that register with the reference frame with a mean correlation (averaged over all strips) greater than a user-selected correlation threshold are included in the final averaged image; frames with a lower correlation are excluded. Typically, 50 to 100 frames are averaged.

Before the OCT spectra are converted to B-scans, a digital dispersion correction is performed, which helps remove any residual dispersion mismatch that may be present in the system.<sup>29</sup> For two-dimensional (2-D) line scan data (obtained when GS1 is not scanning), B-scans are registered using the same strip-wise registration algorithm as the SLO, but with strips slicing the B-scan in the axial direction (see Fig. 2). This registration corrects for both the axial and vertical eye motion; horizontal motion is out of plane with respect to the

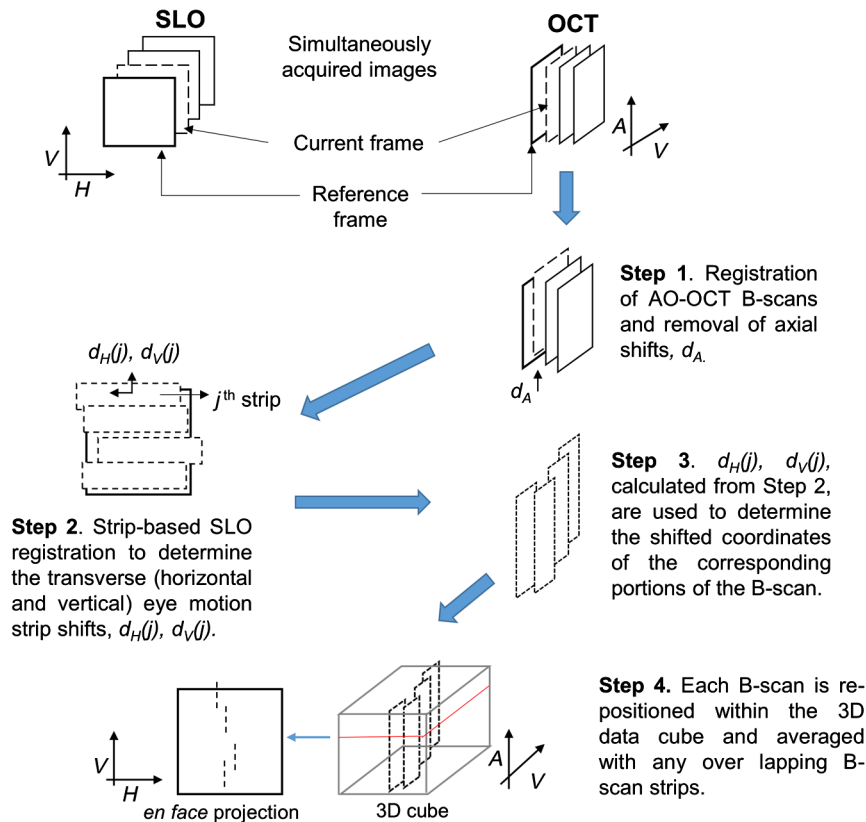


**Fig. 3** Flowchart depicting steps in the 3-D registration of AO-OCT data using transverse shifts measured from AO-SLO frames.

B-scan and thus cannot be monitored. Typically, 10 to 20 B-scans are averaged for line-scan data.

For both the SLO and OCT (2-D) registration, several “good” reference frames (typically  $N = 6$ ) are automatically chosen by a MATLAB routine and used for registration. These  $N$  frames are selected from  $N$  “windows” of equal duration throughout the original video (e.g., if there were 600 frames in the dataset and  $N = 6$ , each window would contain 100 frames), with only one reference frame chosen per window. The auto-registration algorithm selects the  $N$  reference frames based on the mean registration correlation of each frame with its eight neighboring frames (four prior and four subsequent), with a high correlation being preferable. Within each window, the frame with the highest mean correlation with its neighbors is selected. For each selected reference frame, the mean correlation coefficient for that frame in the previous step, minus an offset (typically 0.1), is used as the correlation threshold for averaging (i.e., only frames that register with the reference frame with a mean strip correlation greater than the threshold will be included in the final averaged image). The motivation for this procedure is to help streamline postprocessing and data flow. The auto-selected reference frames do not necessarily represent frames with absolute minimal intra-frame eye motion (i.e., distortion) but are rather intended to be frames to which other frames will register well. The user may choose any of the resulting auto-registered averaged images for subsequent analysis, based on subjective clarity. If none of the auto-registered images are satisfactory (e.g., due to noise, blurring, or poor AO correction), the user may alternatively choose a different reference frame and reregister.

An overview of the 3-D registration procedure for volumetric AO-OCT data is shown in Fig. 3. First, AO-OCT B-scans are axially registered to the reference B-scan using the subpixel registration algorithm developed by Guizar-Sicairos et al.<sup>30</sup> Although this returns both axial and transverse (vertical) shifts, only the axial shift is applied to the B-scan in this step because the resulting transverse shift is not generally reliable, because different cones are depicted in most B-scans. As part of this step, the B-scan is flattened by axially shifting the A-scans such that the photoreceptor layer is aligned to 0 deg (i.e., horizontal). The user may select any reference frame, though one of the auto-registration reference frames is typically chosen. The selected AO-OCT reference frame defines the AO-SLO reference frame for the following registration step (i.e., the AO-SLO frame with the matching frame number, acquired at the same time, is selected).

Next (step 2), the simultaneously acquired AO-SLO frames are registered using the strip-based approach described above to measure transverse eye motion. During this step, the AO-SLO data are used to flag B-scans for exclusion from the 3-D registration (step 3) if: (a) mean intensity of any frame is less than half that of the reference frame (suggestive of a blink); or (b) the standard deviation of the shifts across all strips in that frame is greater than a user-selected threshold, typically 10 pixels (suggesting considerable intraframe eye motion or erroneous registration). If an AO-SLO frame meets either criteria, the simultaneously acquired B-scan (matching frame number) is excluded.

In step 3, the horizontal and vertical shifts measured from the AO-SLO strips [ $d_H(j)$ ,  $d_V(j)$ ] are applied to the corresponding

strips in each B-scan to compensate for transverse eye motion. Each B-scan strip is then placed into the proper position in a 3-D data cube (step 4). Its vertical coordinates are determined by the measured vertical eye motion shift,  $d_V(j)$ , while its horizontal coordinate is a combination of (i) the expected position of the horizontal scan at the time the frame is acquired plus (ii) the measured horizontal eye motion shift,  $d_H(j)$ . For locations with overlapping data, the strips are averaged. B-scans exhibiting sudden eye motion or blinks are excluded from the registration, as described in step 2. After all B-scans have been registered and rendered into a 3-D volume, the user may select any axial depth from which to display an *en face* projection.

## 2.7 Subjects and Imaging

Three healthy subjects (N1, N2, and N3) between the age of 21 to 42 years were imaged. All had visual acuity of 20/15, with refractive errors not exceeding  $-2.75$ -D sphere and  $0.75$ -D cylinder. The presence of abnormal ocular media and retinal disease were ruled out by a conventional eye exam, including slit lamp examination and ophthalmoscopy. The foveal axial length of the eye was measured using the Lenstar LS 900 (Haag-Streit USA, Mason, Ohio). Subjects were dilated with one drop of 1% tropicamide and one drop of 2.5% phenylephrine prior to AO imaging. All subjects had dilated pupils  $\geq 7.15$  mm. A bite bar or a combination of chin and forehead rest were used during imaging to minimize head motion. For all images in this study, focus was set at the photoreceptor layer using a defocus offset applied through the DM. The tenets of the Declaration of Helsinki were observed and the protocol was approved by the Institutional Review Board of The Ohio State University (OSU). Written informed consent was obtained after all procedures were fully explained to the subjects and prior to any experimental measurements.

Instantaneous powers at the cornea were  $<400$   $\mu\text{W}$  for the OCT and  $<60$   $\mu\text{W}$  for the SLO, with the average SLO power reduced to  $<35$   $\mu\text{W}$  due to the AOM. Exposure duration for a single trial was  $\sim 20$  s (including alignment and acquisition), though repeated datasets were taken at some locations with breaks between. Total exposure duration at a single retinal location was typically  $<1$  min, and always  $<5$  min. This results in light exposures well below ANSI safety limits<sup>31</sup> for both volume-scanning ( $0.75$  deg  $\times$   $0.75$  deg) and the more stringent line-scanning mode (1.0 deg).

## 3 Results

### 3.1 System Characterization on a Model Eye

To evaluate system performance, measurements were carried out using a model eye consisting of an  $f = 100$ -mm achromatic lens, pupil iris ( $d = 7.15$  mm), and a diffuse scattering target to simulate the retina. To measure the on-axis aberrations of the optical system, WFS measurements were taken with the DM flattened, scanners turned off, and the retinal target placed in the focal plane of the model eye lens. Figure 4 shows the single-pass Zernike coefficients<sup>32</sup> (up to Z10) and total RMS error measured for the OCT and SLO beams, along with the corresponding values from the Zemax design using the OCT optical path. One reason for the increase in system aberration compared with theory is that the angle of incidence off of the final spherical mirror of the system (SM12) is  $\sim 2$  deg greater than prescribed in Zemax. This is because in implementing the design, a slightly longer working

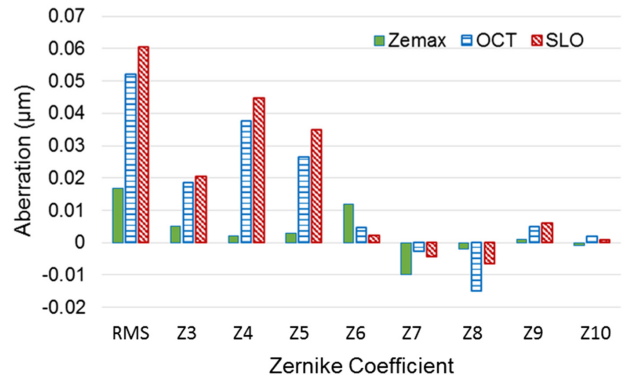


**Fig. 4** Single-pass system aberrations for the OCT (blue, horizontal hash marks) and SLO (red, diagonal hash marks) beams measured with a model eye consisting of an  $f = 100$ -mm lens and a diffuse scattering surface. Aberrations predicted by the Zemax model using the OCT system are shown for comparison (green, solid).

distance was required between the last folding mirror (FM) and the eye to provide sufficient space for the subject positioning assembly and pellicle. Therefore, the last FM was placed  $\sim 4$  cm closer to SM12 than originally designed, requiring an increase in the angle off of SM12 to avoid cropping the beam. There is also  $\sim 10$  nm of uncorrected defocus.

Figure 5 shows (a) the OCT and (b) SLO single-pass point spread functions (PSFs) measured with a CCD camera at the retinal plane of the model eye and scaled for a 17-mm eye. Ideal diffraction-limited PSFs calculated from the center wavelengths of each channel are shown for comparison. It can be seen that the residual system aberrations broaden the OCT and SLO PSFs slightly compared with their respective diffraction-limited Airy patterns, 9% and 24%, respectively, when taking the average of the  $x$ - and  $y$ -profiles at the full width at half maximum (FWHM). The AO-corrected PSFs show slight improvements, 5% and 20% broader than the Airy PSFs for OCT and SLO, respectively. AO-corrected lateral imaging resolution was tested with a USAF resolution test chart. Scaled for a 17-mm focal length eye, the smallest resolvable line pair spacings were  $2.3$   $\mu\text{m}$  for the OCT and  $1.9$   $\mu\text{m}$  for the SLO (using a 1 Airy disk pinhole).

The FWHM OCT axial resolution measured using a glass slide in the sample arm and neutral density filters to prevent saturation was  $\sim 2.2$   $\mu\text{m}$  (adjusted for retinal tissue,  $n = 1.38$ ), compared with the theoretical value of  $\sim 1.7$   $\mu\text{m}$ . Sensitivity of the OCT was measured using a glass slide in the sample arm. For the case of volume scanning over a  $0.75$  deg  $\times$   $0.75$  deg FOV, sensitivity was calculated to be 91 dB when the slide was positioned with the reflectance peak near the top of the image and 89 dB at a depth of  $500$   $\mu\text{m}$ , which is a typical axial depth for the photoreceptor layer. Sensitivity roll off was  $\sim 4$  dB/mm.

### 3.2 Retinal Imaging in Human Eyes

To demonstrate the resolution and imaging capabilities of the AO-OCT-SLO system *in vivo*, images were acquired on all three subjects at the fovea, 5-deg TR, 10-deg TR, and 15-deg TR, respectively. A confocal SLO pinhole equal to 1.0 Airy disk diameter was used throughout.

#### 3.2.1 Lateral resolution—foveal cone imaging

Foveal cones diameters are  $\sim 2.5$   $\mu\text{m}$  with a regular packing arrangement, which provides an ideal test of a system's lateral

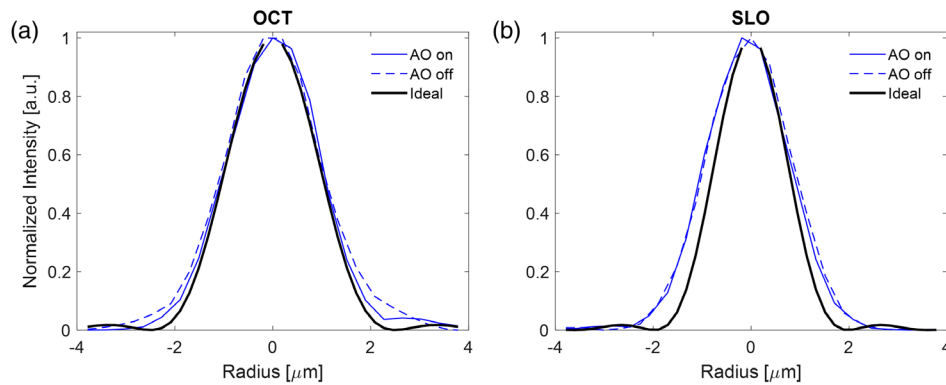


**Fig. 5** Single-pass system PSFs measured at the model eye retinal plane. Radial units are scaled for an  $f = 17\text{-mm}$  eye. (a) OCT: PSF profile in the  $x$ -direction with AO on (solid blue line); profile in the  $x$ -direction with AO off (dashed blue line); and the diffraction-limited PSF (black bold line). (b) SLO: PSF profile in the  $x$ -direction with AO on (solid blue line); profile in the  $x$ -direction with AO off (dashed blue line); and the diffraction-limited PSF (black bold line). PSF profiles in the  $y$ -direction are similar and not shown for clarity.

resolution. Figure 6 shows AO-OCT and AO-SLO results from all three subjects at the fovea with the OCT operating in line-scan mode and focus set at the level of the photoreceptors. The yellow dashed lines indicate the position of the OCT B-scan with respect to the SLO. For each subject, cones can be resolved throughout most, though not the entirety, of the SLO images, with a clear breakup of the inner segment–outer segment junction (IS/OS) in the OCT images. Minimum cone spacing that could be reliably measured in the AO-SLO images, taken as the average nearest-neighbor spacing

in the regions shown in the blue boxes ( $\sim 30 \times 30 \mu\text{m}^2$ ), were 2.7, 3.0, and  $3.1 \mu\text{m}$ , for subjects N1 to N3 respectively, in reasonable agreement with the resolution limits detailed previously.

### 3.2.2 Axial measurement of cone and rod microstructure

Figure 7(a–h) shows the AO-OCT and corresponding AO-SLO images from subject N1 at each of the four retinal locations, with the smaller rods visible between cones at some locations in the

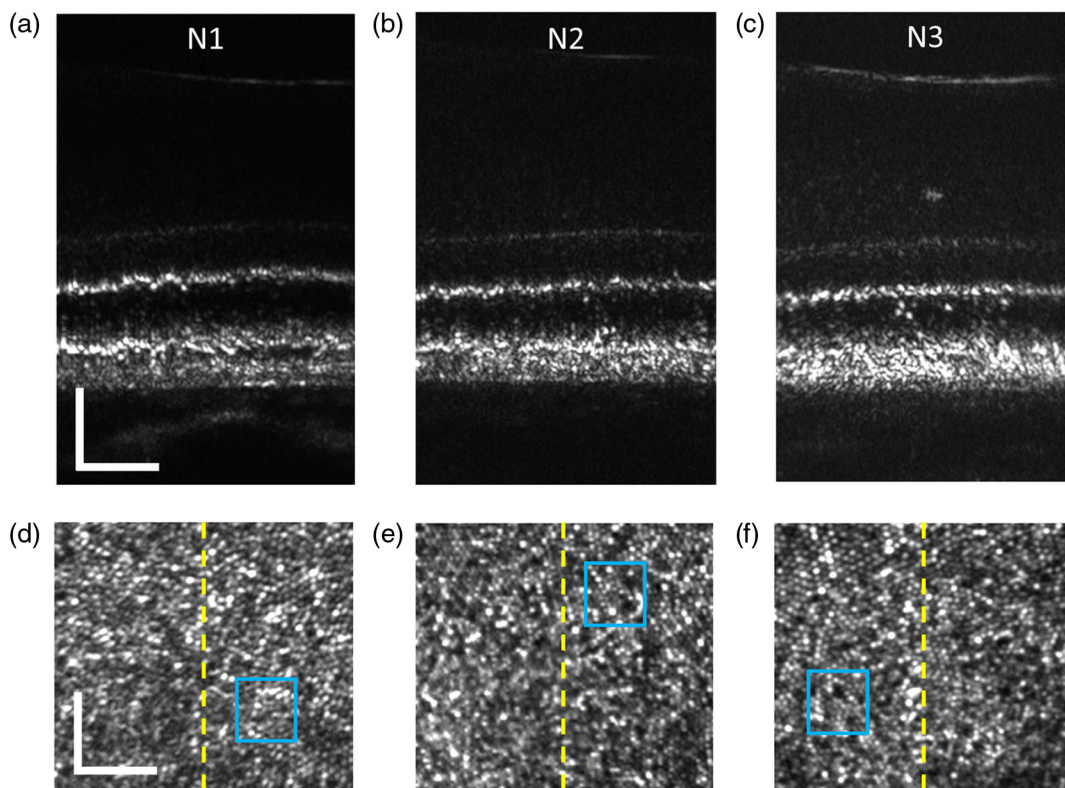


**Fig. 6** (a)–(c) AO-OCT and (d)–(f) AO-SLO images of the fovea from three control subjects. The AO-OCT images are averages of  $\sim 10$  registered B-scans; the AO-SLO images are averages of  $\sim 100$  registered SLO frames. The dashed lines in the AO-SLO images indicate the orientation of the AO-OCT B-scan, and the blue boxes are the regions over which cone spacing was calculated. All images are shown with linear intensity scaling. Scale bars =  $50 \mu\text{m}$ .

temporal AO-SLO images. To investigate differences between the cone and rod axial reflectance profiles in the AO-OCT B-scans at the different retinal eccentricities, the following analysis was performed. First, tilt was removed in the registered B-scan by axially shifting the A-scans such that the photoreceptor layer is aligned at 0 deg (i.e., horizontal). Cones are then manually identified based on the observation of bright reflectance peaks near the IS/OS junction with matching (aligned in the transverse direction) cone outer segment tip (COST) reflectance. Only the central few A-scans were included for analysis for each cone (1, 3, 5, and 5 A-scans for images at the fovea, 5 deg, 10 deg, and 15 deg, respectively). A buffer region of 3 A-scans on either side of each cone was then excluded (with

the exception of at the fovea) to help prevent misclassification due to potential edge effects (such as blurring or tilting). These lines were not classified as either a cone or rod. All remaining A-scans lines were classified as “rod” structure, based on the assumption that regions surrounding the cones comprise rods, as observed in SLO images and histology.<sup>33</sup> As a final step, the user has the option to exclude any additional A-scans that appear ambiguous or misidentified. The most common scenarios were IS/OS spots missing an aligned COST reflection, or vice versa.

Selected A-scans for the two types of photoreceptor were averaged to generate axial reflectance profiles. Peaks corresponding to the following anatomical structures were manually

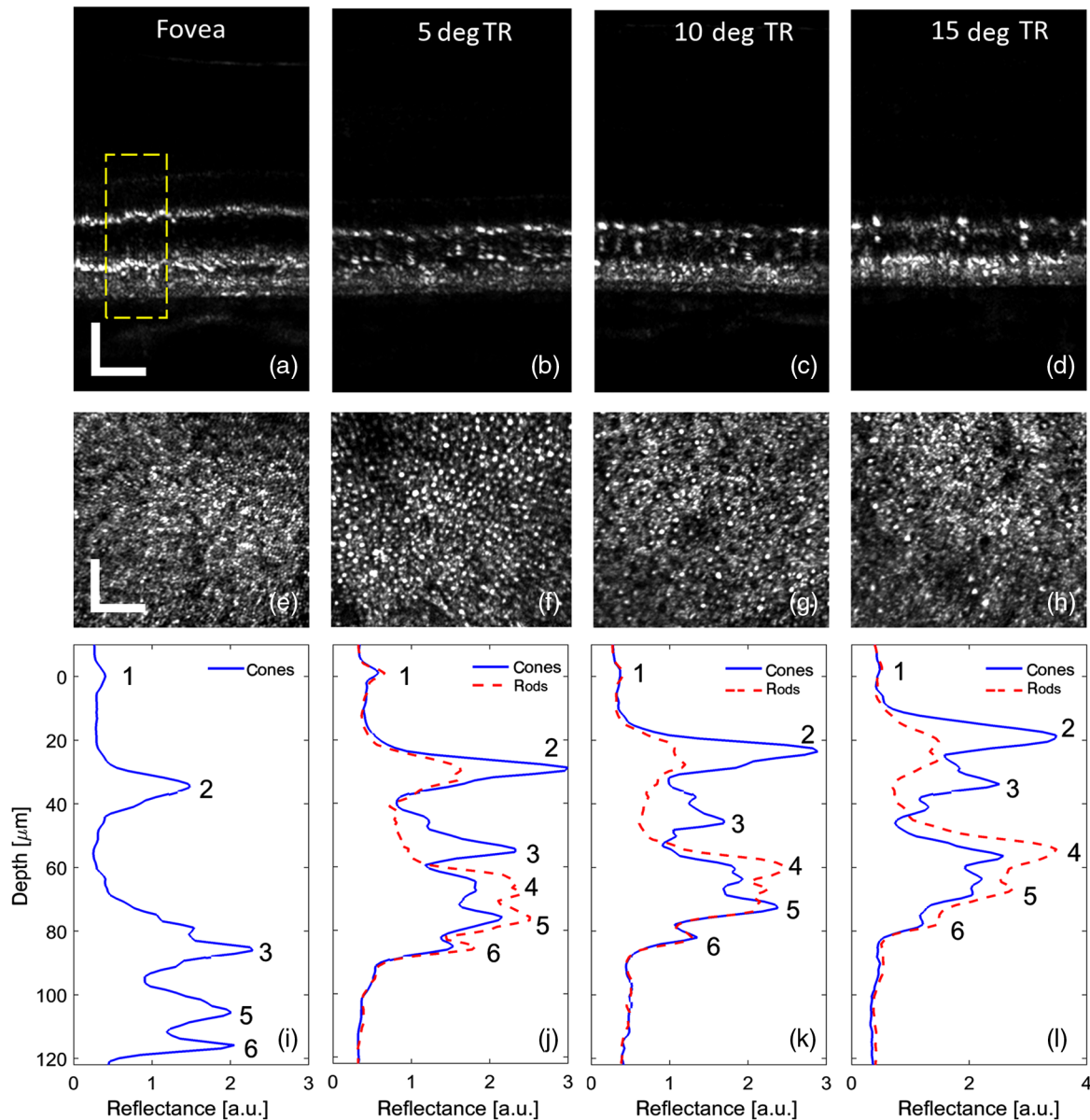


**Fig. 7** (a)–(d) AO-OCT and (e)–(h) AO-SLO images from subject N1 at the fovea, 5-deg TR, 10-deg TR, and 15-deg TR. The AO-OCT images are an average of  $\sim 10$  registered B-scans; the AO-SLO images are averages of  $\sim 50$  registered SLO frames. All images are displayed with linear intensity scaling. (i)–(l) The cone (blue solid line) and rod (red dashed line) mean axial profiles for each imaging location, with ELM plotted at  $0\text{-}\mu\text{m}$  depth in all images for comparison. The numbered peaks correspond to: 1. ELM, 2. IS/OS junction, 3. COST, 4. ROST, 5. RPE, and 6. BM. For the foveal location, only a subset of cones,  $\sim 0.25$  deg from the foveal pit, were measured (yellow dashed box, top). Scale bars =  $50\ \mu\text{m}$ .

identified: (1) external limiting membrane (ELM), (2) inner segment–outer segment junction (IS/OS), (3) COST, (4) rod outer segment tips (ROST), (5) retinal pigment epithelium (RPE), and (6) Bruch’s membrane (BM). COST and ROST were identified only for cones and rods, respectively; all other peaks were identified for both. For cones, the following calculations were made based on the positions of these peaks: inner segment length (ISL; distance from the ELM to IS/OS), outer segment length (OSL; distance from IS/OS to COST), and the distance from the COST to the RPE. For rods, ISL, OSL (distance from IS/OS to ROST), and distance from the ROST to the RPE were measured. Figure 7(i–l) shows the cone and rod axial reflectance profiles for subject N1 for the corresponding registered averaged B-scans, with the ELM peak plotted at the 0- $\mu\text{m}$  position in all images for comparison.

To investigate reproducibility of the axial profiles across different AO-OCT B-scans, we repeated the 10-deg temporal measurements shown in Fig. 7 for five additional B-scans from subject N1. All six images were acquired at the same retinal location but each depicted different individual cones due to eye motion. Each image was the registered average of between 4 and 13 individual B-scans (mean = 8) and each contained between 8 to 12 cones (mean = 10). Peaks were identified and segment lengths calculated and results compared across images. The positions of the peaks, as well as the calculated ISL and OSL for cones and rods, were found to show a high degree of repeatability across B-scans. All peaks, with exception of the COST (peak 3), had a standard deviation  $\leq 2.3 \mu\text{m}$ . The comparatively large standard deviation among COST peak position ( $3.4 \mu\text{m}$ ) may be due to the inherent variance in the actual lengths of cone outer segments. Spurious reflections that sometimes occur within the cone outer segment in AO-OCT images may also be a contributing factor.

The axial measurements averaged across all three subjects are shown in Table 2, along with histological findings from Spaide and Curcio<sup>33</sup> at the fovea and 7 deg for comparison. Results tended to be in good agreement with histology. Generally, ISL and OSL decreased for both cones and rods with increasing eccentricity. On average, rod ISL was slightly longer than cone ISL at the two highest eccentricities, though a similar trend was not observed at 5-deg TR. Due to the small sample size, these results were not statistically significant. Interestingly, cone ISL at the fovea was in good agreement with the Spaide and Curcio model, but the OSL was significantly (22%) longer. The COST–RPE distance agrees well with histology; however, the ROST–RPE distance of  $9.9 \mu\text{m}$  is on the order

of the length of RPE microvilli ( $5$  to  $7 \mu\text{m}$ ), suggesting that the ROST band may originate from the proximal end of the RPE apical extension/microvilli that surrounds the distal end of the rod OS.

In a separate, single imaging session, subject N3 was imaged from 1 deg inferior retina (IR) to 20 deg superior retina (SR) in 0.5 deg increments. Figure 8 shows the stitched AO-OCT and AO-SLO images from the entire region, demonstrating the continuous and gradual change in photoreceptor structure from the fovea to midperiphery. All images were first individually registered and averaged ( $\sim 50$  to  $100$  for SLO,  $\sim 10$  to  $20$  for OCT) prior to forming the montages. AO-SLO images were manually stitched together using cones and vasculature as landmarks. The AO-OCT is not a true montage; due to an  $\sim 1$ -deg tilt in the vertical scan orientation, the “overlap” regions at the margins of successive B-scans cannot be registered to form a continuous image. As a result, discontinuities are present between individual B-scans, most notable at the photoreceptor layer.

### 3.2.3 Three-dimensional volumetric imaging

Figure 9 shows (a) AO-SLO and (b–f) AO-OCT images from subject N3 at 10 deg TR acquired with the OCT in volume-scanning mode. The FOV was set to  $0.75 \text{ deg} \times 0.75 \text{ deg}$ . The AO-OCT images are reconstructed *en face* projections from different axial depths in the 3-D OCT volume, which was rendered using the measured SLO transverse eye motion to register the OCT B-scans. Retinal layers corresponding to the following structures are shown: (c) IS/OS junction, (d) COST, (e) ROST, and (f) RPE. These results were reconstructed from a single volume of OCT/SLO data (i.e., no volume averaging). Figure 9(g) is a false color image with the COST layer (red) overlaid on the ROST layer (green), and the area within the yellow dashed box is shown in (h). The vertical black lines in the images are the result of eye motion during the volume scan, which causes gaps between adjacent B-scans at certain locations. Gaps of 3 pixels or less were filled in for display purposes by interpolating the pixel intensity values of the nearest data to the left and right. Each image is the average over a depth of three pixels ( $\sim 3 \mu\text{m}$ ). No averaging or filtering was performed laterally, aside from the aforementioned interpolation.

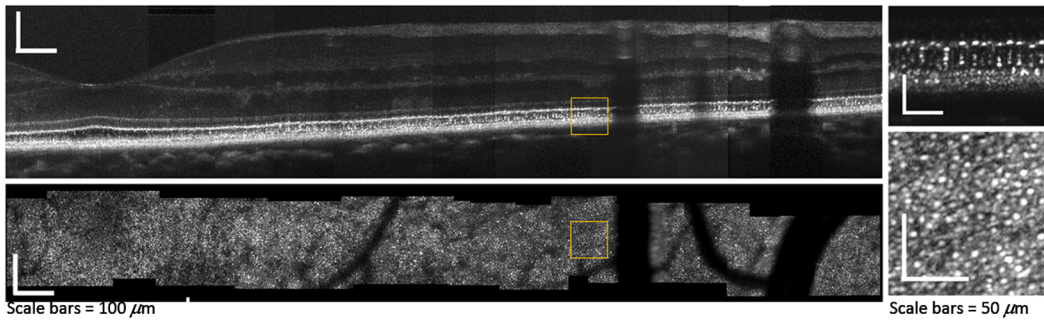
In line-scanning mode (with the OCT volume-scanning galvo, GS1, turned off), eye motion causes the OCT line scan to traverse a region of the retina around the target imaging location. Because of this motion, even with the volume scanner turned off, it is possible to use the SLO measured shifts to reconstruct a 3-D

**Table 2** Cone and rod axial measurements from AO-OCT reflectance profiles.

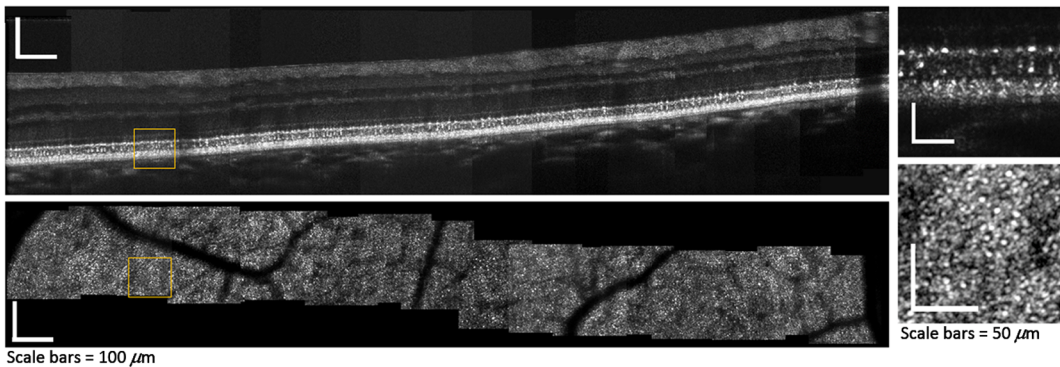
Location	Cone ISL ( $\mu\text{m}$ )	Cone OSL ( $\mu\text{m}$ )	Rod ISL ( $\mu\text{m}$ )	Rod OSL ( $\mu\text{m}$ )	COST-ROST ( $\mu\text{m}$ )	COST-RPE ( $\mu\text{m}$ )	ROST-RPE ( $\mu\text{m}$ )
Fovea	$35.8 \pm 1.7$	$42.7 \pm 3.3$				$17.1 \pm 1.9$	
5-deg TR	$29.5 \pm 2.5$	$23.9 \pm 1.6$	$29.7 \pm 2.7$	$35.5 \pm 1.6$	$11.6 \pm 1.6$	$21.9 \pm 0.6$	$9.9 \pm 0.6$
10-deg TR	$24.6 \pm 2.8$	$21.9 \pm 1.2$	$26.7 \pm 0.1$	$33.1 \pm 1.2$	$11.3 \pm 2.1$	$24.9 \pm 2.1$	$11.3 \pm 3.1$
15-deg TR	$24.3 \pm 3.1$	$17.8 \pm 4.2$	$26.3 \pm 1.2$	$32.7 \pm 2.8$	$14.9 \pm 1.9$	$27.7 \pm 4.7$	$10.4 \pm 3.4$
Fovea <sup>a</sup>	34	35					
7-deg TR <sup>a</sup>	29	—	29	32		20	<1

<sup>a</sup>Bottom two rows are from Spaide and Curcio.<sup>33</sup>

## (a) 1 deg IR to 6 deg SR



## (b) 5.5 deg SR to 13 deg SR



## (c) 13 deg SR to 20 deg SR

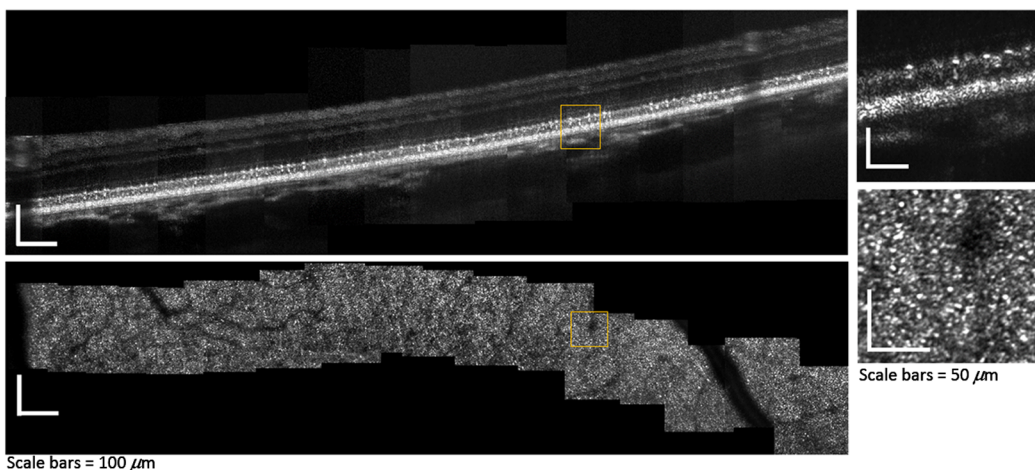


**Fig. 8** Stitched montages of AO-OCT (top) and AO-SLO (bottom) images from subject N3, ranging from (a) 1-deg IR to 6-deg SR; (b) 5.5-deg SR to 13-deg SR; and (c) 13-deg SR to 20-deg SR. Yellow boxes indicate locations of the zoomed-in regions shown on the right and are located at (a) 4-deg SR, (b) 7-deg SR, and (c) 18-deg SR. OCT images are displayed with logarithmic intensity scaling for the main stitched images, and linearly for the insets. All SLO images are displayed linearly. Scale bars for the montages are 100 and 50  $\mu\text{m}$  for the expanded regions.

AO-OCT dataset. As an example, Fig. 10(a) shows an AO-SLO image from subject N1 at 1-deg SR. Figure 10(b) shows the corresponding COST layer *en face* projection from the 3-D OCT data, which was registered using the eye motion shifts obtained during the registration of (a). Figures 10(c) and 10(d) show zoomed-in views of (b) and (a), respectively. Similar to the data shown in Fig. 9 that were acquired in volume-scanning mode, gaps can be seen in the registered OCT images in Figs. 10(b) and 10(c). The horizontal extent of the registered OCT volume

shown here is  $\sim 0.12$  deg, roughly the extent of horizontal eye movement during this trial. This volume was registered from 260 individual B-scans. Acquiring more frames would potentially allow larger volumes to be registered. This approach could be adapted by intentionally moving the fixation target and creating volumes of larger FOV than either those shown here or in Fig. 8. This could be accomplished without a separate OCT volume-scanning galvo, which would have the potential to simplify the system design.

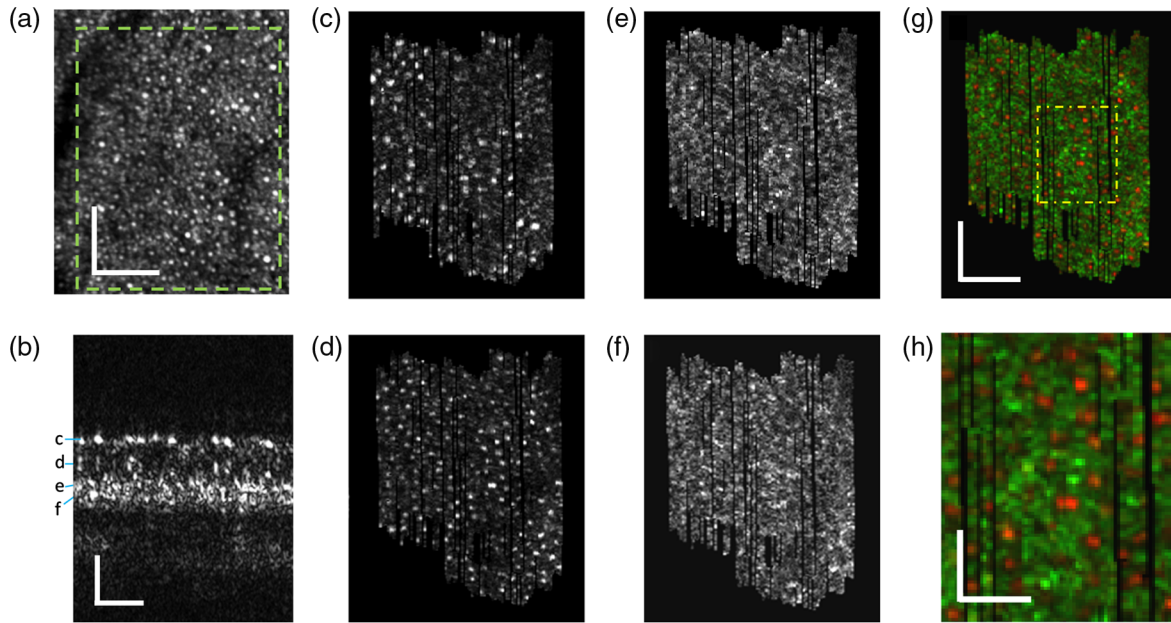


**Fig. 9** Volumetric data acquired from the combined AO-OCT-SLO system at 10-deg TR in subject N3, with OCT *en face* projections at key retinal layers. (a) Registered SLO image, average of 50 frames, with the dashed box indicating the region corresponding to the registered OCT data; (b) a single B-scan (no averaging) indicating the axial positions of the layers shown in the subsequent panels; (c) IS/OS junction; (d) COST; (e) ROST; (f) RPE; (g) false color overlay image with COST displayed in red and ROST green; and (h) expanded view of the dashed box shown in (g). Vertical black lines in the OCT *en face* images are an artifact of eye motion. Scale bars in (a), (b), and (g) are 50  $\mu\text{m}$ , and (h) 20  $\mu\text{m}$ .

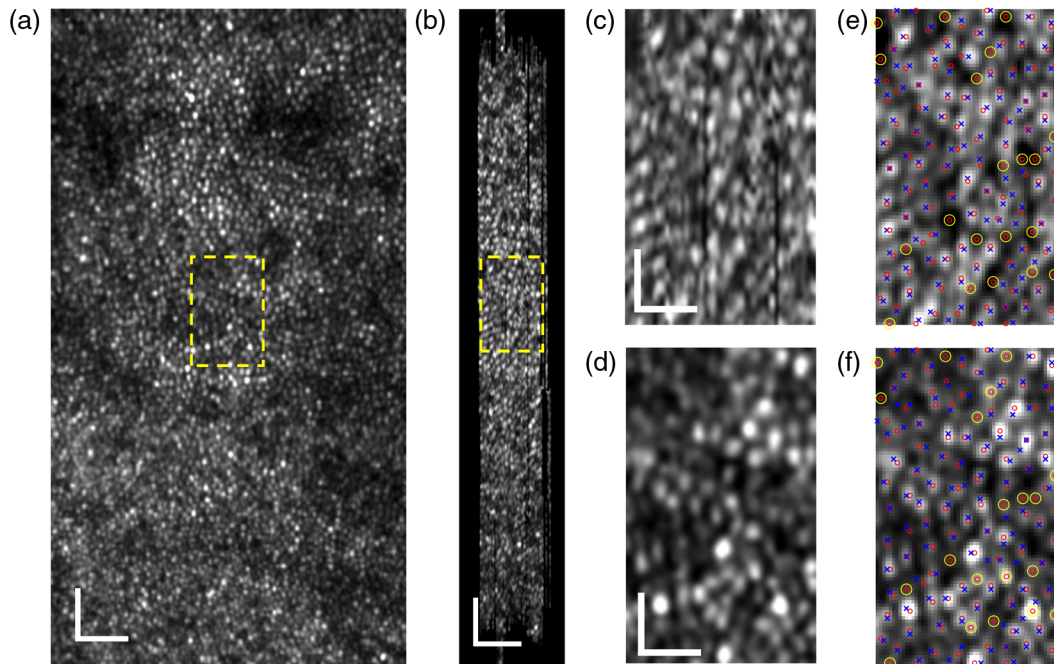


**Fig. 10** 3-D registration of images from N3 at 1-deg SR acquired in line-scanning mode, using only eye motion to scan the OCT beam in the horizontal direction; (a) registered AO-SLO image from which the *x*- and *y*-directions (horizontal and vertical) eye motion was measured; (b) *en face* projection of the COST layer taken from the registered AO-OCT volume; (c) zoomed-in OCT image from the yellow dashed box in (b); and (d) zoomed-in SLO image from the yellow dashed box in (a). Scalebars are 25  $\mu\text{m}$  in (a) and (b), and 10  $\mu\text{m}$  in (c) and (d). (e) Same AO-OCT image as (c) after Gaussian blurring ( $\sigma = 1$  px,  $\sim 0.5 \mu\text{m}$ ), and (f) same AO-SLO image as (d). In (e) and (f), red circles denote positions of cones identified in the AO-SLO and blue X's denote positions of cones identified in the AO-OCT. Yellow circles show SLO-identified cones that do not have a matching OCT-identified cone within three pixels ( $\sim 1.5 \mu\text{m}$ ).

A similar cone mosaic can be seen in the AO-OCT and AO-SLO images in Figs. 10(c) and 10(d). Applying a semiautomated cone identification routine<sup>34</sup> to both images, which includes low-pass filtering with a  $\sigma = 1$  pixel ( $\sim 0.5 \mu\text{m}$ ) Gaussian filter, results in 109 cones identified in the AO-OCT and 119 in the AO-SLO images. The identified cone positions are marked by blue (OCT-identified) and red (SLO-identified) markers in both the AO-OCT [Fig. 10(e)] and AO-SLO [Fig. 10(f)] images for comparison. Of the SLO-identified cones, 99 (83%) had a “matching” OCT-identified cone within a distance of  $1.5 \mu\text{m}$ . Of the 20 SLO-identified cones without an OCT match (circled in yellow), most corresponded to low-intensity regions of both the SLO and OCT images, which can lead to inaccuracies in identifying the centers of cells. Several ( $\sim 10$ ) appear to be very dim cones, which are detected in the SLO, but are not visible in the OCT. The Pearson’s correlation coefficient between the two images is 0.33. This moderate correlation reflects the degrading effect of registration and eye motion artifacts in the AO-OCT image as well as inherent imaging differences between the two modalities (e.g., different imaging wavelengths, different axial resolutions, and coherent versus incoherent detection). The relative intensity of a cone in the AO-SLO does not generally correlate well with that of the AO-OCT.

#### 4 Discussion and Conclusions

We have implemented a newly designed, out-of-plane, dual-modality AO imaging system with simultaneous OCT and SLO acquisition that has the ability to acquire 3-D retinal volumes. To demonstrate system performance and *in vivo* resolution, AO-corrected images obtained in OCT line-scan mode were presented from three control subjects ranging from the fovea to the near periphery (0-deg to 15-deg TR;  $-1$ -deg IR to 20-deg SR), at larger retinal eccentricities than prior published reports. Although cones were resolved across all eccentricities and modalities including near the fovea, rods were only resolved at certain locations in the AO-SLO images (for example, 10-deg TR in Fig. 7). In the AO-OCT images, rod structure could be observed in the ring-like pattern in the *en face* ROST projection [Fig. 9(e)] and the relatively dim IS/OS junction reflectance occurring between neighboring cones [Figs. 7 and 9(c)].

The approach used here for registering 3-D AO-OCT volumes uses the transverse eye motion obtained from AO-SLO strip-based registration<sup>28</sup> to properly position the 2-D AO-OCT B-scans. While other studies have used a similar approach,<sup>10,35</sup> the algorithm used here was independently developed along with the current system. This approach is in contrast with stand-alone AO-OCT 3-D imaging,<sup>6,15–17,19</sup> which typically relies on high acquisition speed or dynamic eye tracking to mitigate eye motion artifacts. Kocaoglu et al.<sup>20</sup> recently implemented an AO-OCT system with 1-MHz A-scan rate capable of producing *en face* projections of retinal layers including COST, IS/OS junction, and RPE. While the high speed offered by such systems allows AO-OCT registration without the need for SLO due to reduced eye motion between B-scans, one trade-off is sensitivity, requiring registration and averaging of multiple volumes to increase the signal-to-noise. The system described here acquires volumes slowly by comparison ( $\sim 4.2$  s) but has relatively high sensitivity and can therefore produce clear images of retinal structures with only a single volume. One advantage to this approach is a reduction in data storage and

computer processing time, because fewer volumes are required. Aside from the initial AO-SLO registration, which may take 1 to 15 min depending on how many reference frames are tested and the precision of the registration, the volume registration is performed in  $<1$  min.

The benefits of faster volume acquisition ( $\sim 4.2$  s), as compared with previous combined AO-OCT-SLO systems with a similar scanning configuration<sup>35</sup> ( $\sim 7$  s), relate to ease of imaging. It is desirable to acquire volumes relatively quickly to reduce subject blinking and tear film breakup, both which have a deleterious effect on AO correction. While an even shorter volume acquisition time would be beneficial, with the current system design, the B-scan acquisition rate is tied to the SLO frame rate (60 Hz) due to the shared galvo, GS2, which limits how fast AO-OCT volumes can be acquired. Using separate scanning mirrors for both the SLO and OCT is possible but at the cost of greater system complexity.

Imaging speed and axial resolution are a tradeoff in OCT because the broader the source spectrum the more spectrometer pixels must be read out. In the current configuration, with  $\lambda_c = 860$  nm and  $\Delta\lambda = 140$  nm, we use 2024 pixels, which is half the 4048 available on the Basler Sprint spectrometer camera. Although the system could operate faster using fewer pixels, the current arrangement allows us to take full advantage of the ultrahigh axial resolution capabilities of the broadband SLD source. With a theoretical axial resolution in tissue of  $1.7 \mu\text{m}$ , the AO-OCT subsystem has one of the best nominal axial resolutions of any current AO imaging system.

Although we have not directly measured the precision of the 3-D registration algorithm, we note that at 1 deg from the fovea, 83% of SLO-identified cones have OCT-identified cones appearing at matching locations ( $<1.5 \mu\text{m}$  separation) in the OCT *en face* projection image [Figs. 10(e) and 10(f)]. We cannot be sure to what extent the slight differences in cone position between the two images is due to registration artifacts (i.e., lack of precision), as opposed to inherent differences between OCT and SLO imaging modalities. However, based on the registration artifacts visible in the unfiltered *en face* AO-OCT image in Fig. 10(c), we estimate the precision to be on the order of 1 to  $2 \mu\text{m}$  (approximately one-third to one-half the diameter of a cone).

The ability to obtain high-resolution retinal images beyond the macula and into the periphery<sup>36</sup> is significant in the detection and monitoring of diseases, such as retinitis pigmentosa and cone-rod dystrophy, among others. There are two limitations when imaging at large eccentricities. First, the effective diameter of the pupil decreases; while this is not a significant limitation for young, healthy subjects with large dilated pupils, it can be an issue for older subjects and those whose ocular condition precludes full dilation. The second is the increase in astigmatism as the beam enters the eye at increasingly oblique angles, which can be several diopters in magnitude.<sup>37</sup> If left uncorrected, this can be a burden on the DM. However, because the aberrations introduced by eccentric imaging are mostly contained in the 90 deg astigmatism coefficient (Z5), it is relatively straightforward to correct this using a properly aligned trial lens. Trial lenses were not used in this study to correct for these aberrations, likely contributing to a slight decrease in AO-corrected resolution at the more eccentric regions of Fig. 8.

The algorithm for 3-D registration is currently being refined, including implementation of subpixel registration, which may improve visualization of small structures (such as rods) in the

en face images. Although the AO-OCT images in Fig. 9 are from only a single volume, averaging several datasets is expected to be beneficial for removing the gaps in the data that result from eye motion. This would make subpixel volume registration feasible, further enhancing resolution. Subpixel registration is possible with only a single volume, but it increases the gaps (the vertical black lines) in the rendered 3-D volumes. Another benefit of averaging several OCT volumes acquired at different time points is the ability to reduce speckle contrast. This has been shown to greatly improve visibility of cellular structures in RPE and retinal nuclear layers and might allow estimation of intracellular motility, a possible biomarker of cell health.<sup>38</sup>

### Disclosures

The authors have no relevant financial interests in this article and no potential conflicts of interest to disclose.

### Acknowledgments

This work was supported by Department of Defense (DoD) Telemedicine and Advanced Technology Research Center (TATRC) grant W81XWH-10-1-0738 and National Institutes of Health (NIH) grants EY020901 and EY024239.

### References

- J. Liang, D. R. Williams, and D. T. Miller, "Supernormal vision and high-resolution retinal imaging through adaptive optics," *J. Opt. Soc. Am. A* **14**(11), 2884–2892 (1997).
- A. Roorda et al., "Adaptive optics scanning laser ophthalmoscopy," *Opt. Express* **10**(9), 405–412 (2002).
- D. T. Miller et al., "Coherence gating and adaptive optics in the eye," *Proc. SPIE* **4956**, 65–72 (2003).
- B. Hermann et al., "Adaptive-optics ultrahigh-resolution optical coherence tomography," *Opt. Lett.* **29**(18), 2142–2144 (2004).
- Y. Zhang et al., "Adaptive optics parallel spectral domain optical coherence tomography for imaging the living retina," *Opt. Express* **13**(12), 4792–4811 (2005).
- R. J. Zawadzki et al., "Adaptive-optics optical coherence tomography for high-resolution and high-speed 3D retinal in vivo imaging," *Opt. Express* **13**(21), 8532–8546 (2005).
- A. G. Podoleanu and D. A. Jackson, "Combined optical coherence tomograph and scanning laser ophthalmoscope," *Electron. Lett.* **34**(11), 1088–1090 (1998).
- D. Merino et al., "Adaptive optics enhanced simultaneous en-face optical coherence tomography and scanning laser ophthalmoscopy," *Opt. Express* **14**(8), 3345–3353 (2006).
- M. Pircher et al., "Simultaneous imaging of human cone mosaic with adaptive optics enhanced scanning laser ophthalmoscopy and high-speed transversal scanning optical coherence tomography," *Opt. Lett.* **33**(1), 22–24 (2008).
- F. Felberer et al., "Adaptive optics SLO/OCT for 3D imaging of human photoreceptors in vivo," *Biomed. Opt. Express* **5**(2), 439–456 (2014).
- M. Mujat et al., "High resolution multimodal clinical ophthalmic imaging system," *Opt. Express* **18**(11), 11607–11621 (2010).
- A. Meadway, C. A. Girkin, and Y. Zhang, "A dual-modal retinal imaging system with adaptive optics," *Opt. Express* **21**(24), 29792–29807 (2013).
- R. J. Zawadzki et al., "Integrated adaptive optics optical coherence tomography and adaptive optics scanning laser ophthalmoscope system for simultaneous cellular resolution in vivo retinal imaging," *Biomed. Opt. Express* **2**(6), 1674–1686 (2011).
- D. X. Hammer et al., "Multimodal adaptive optics retinal imager: design and performance," *J. Opt. Soc. Am. A* **29**(12), 2598–2607 (2012).
- Y. Zhang et al., "High-speed volumetric imaging of cone photoreceptors with adaptive optics spectral-domain optical coherence tomography," *Opt. Express* **14**(10), 4380–4394 (2006).
- C. Torti et al., "Adaptive optics optical coherence tomography at 120,000 depth scans/s for non-invasive cellular phenotyping of the living human retina," *Opt. Express* **17**(22), 19382–19400 (2009).
- S. H. Lee, J. S. Werner, and R. J. Zawadzki, "Improved visualization of outer retinal morphology with aberration cancelling reflective optical design for adaptive optics—optical coherence tomography," *Biomed. Opt. Express* **4**(11), 2508–2517 (2013).
- R. J. Zawadzki et al., "Adaptive optics-optical coherence tomography: optimizing visualization of microscopic retinal structures in three dimensions," *J. Opt. Soc. Am. A* **24**(5), 1373–1383 (2007).
- O. P. Kocaoglu et al., "Adaptive optics optical coherence tomography with dynamic retinal tracking," *Biomed. Opt. Express* **5**(7), 2262–2284 (2014).
- O. P. Kocaoglu et al., "Adaptive optics optical coherence tomography at 1 MHz," *Biomed. Opt. Express* **5**(12), 4186–4200 (2014).
- R. H. Webb and G. W. Hughes, "Scanning laser ophthalmoscope," *IEEE Trans. Biomed. Eng.* **BME-28**(7), 488–492 (1981).
- R. H. Webb, G. W. Hughes, and F. C. Delori, "Confocal scanning laser ophthalmoscope," *Appl. Opt.* **26**(8), 1492–1499 (1987).
- S. A. Burns et al., "Large-field-of-view, modular, stabilized, adaptive-optics-based scanning laser ophthalmoscope," *J. Opt. Soc. Am. A* **24**(5), 1313–1326 (2007).
- A. Dubra and Y. Sulai, "Reflective afocal broadband adaptive optics scanning ophthalmoscope," *Biomed. Opt. Express* **2**(6), 1757–1768 (2011).
- A. Gómez-Vieyra et al., "First-order design of off-axis reflective ophthalmic adaptive optics systems using afocal telescopes," *Opt. Express* **17**(21), 18906–18919 (2009).
- R. E. Bedford and G. Wyszecki, "Axial chromatic aberration of the human eye," *J. Opt. Soc. Am.* **47**(6), 564–565 (1957).
- R. J. Zawadzki et al., "Ultrahigh-resolution optical coherence tomography with monochromatic and chromatic aberration correction," *Opt. Express* **16**(11), 8126–8143 (2008).
- S. B. Stevenson and A. Roorda, "Correcting for miniature eye movements in high resolution scanning laser ophthalmoscopy," *Proc. SPIE* **5688**, 145–151 (2005).
- M. Wojtkowski et al., "Ultrahigh-resolution, high-speed, Fourier domain optical coherence tomography and methods for dispersion compensation," *Opt. Express* **12**(11), 2404–2422 (2004).
- M. Guizar-Sicairos, S. T. Thurman, and J. R. Fienup, "Efficient subpixel image registration algorithms," *Opt. Lett.* **33**(2), 156–158 (2008).
- American National Standard for Safe Use of Lasers*, American National Standards Institute (ANSI), Orlando, Florida (2014).
- Ophthalmics—Methods of Reporting Optical Aberrations of Eyes Z80.28-2010*, American National Standards Institute (ANSI), Washington, DC (2010).
- R. F. Spaide and C. A. Curcio, "Anatomical correlates to the bands seen in the outer retina by optical coherence tomography: literature review and model," *Retina* **31**(8), 1609–1619 (2011).
- B. Xue et al., "Photoreceptor counting and montaging of en-face retinal images from an adaptive optics fundus camera," *J. Opt. Soc. Am. A* **24**(5), 1364–1372 (2007).
- R. J. Zawadzki et al., "Progress on developing adaptive optics-optical coherence tomography for in vivo retinal imaging: monitoring and correction of eye motion artifacts," *IEEE J. Sel. Top. Quantum Electron.* **20**(2), 322–333 (2014).
- E. M. Wells-Gray et al., "Variation in rod and cone density from the fovea to the mid-periphery in healthy human retinas using adaptive optics scanning laser ophthalmoscopy," *Eye* **30**(8), 1135–1143 (2016).
- J. Gustafsson et al., "Peripheral astigmatism in emmetropic eyes," *Ophthalmic Phys. Opt.* **21**(5), 393–400 (2001).
- Z. L. Liu et al., "Characterizing motility dynamics in human RPE cells," *Proc. SPIE* **10045**, 1004515 (2017).

**Elaine M. Wells-Gray** is a senior research associate at the Ohio State University College of Optometry. She received her BS in Biomedical Engineering from the University of Iowa in 2003, and she earned her PhD in biomedical engineering with a focus in biomedical optics from Oregon Health and Science University in 2011. Her research interests include advanced imaging techniques, computational image processing, and their biological applications. She is a member of SPIE.

**Stacey S. Choi** is an associate professor at the College of Optometry and also at the Department of Ophthalmology and Visual Science at the Ohio State University (OSU). Her research interests are clinical application of high-resolution retinal imaging systems including adaptive optics to study underlying disease mechanisms through *in vivo* imaging of human retina. She received her PhD in vision science from the University of Auckland, New Zealand and performed postdoctoral and subsequent research work at the Universities of California at Berkeley and Davis, and also at the University of Rochester, New York, USA.

**Robert J. Zawadzki** is an associate research professor in the Department of Ophthalmology and Visual Science at the University of California, Davis. His research is focused on development and application of high-resolution retinal imaging instruments to study retinal structure and function in normal aging and disease in humans and animal models of human diseases. He received his PhD in natural sciences from Technical University of Vienna, Austria and performed postdoctoral and subsequent research work at University of California, Davis.

**Susanna C. Finn** is a research scientist at the Lowell Center for Space Science and Technology at the University of Massachusetts Lowell. She received her bachelor of science in physics from Brown University, and her PhD in astronomy from Boston University. She performed postdoctoral research at the New England College of Optometry (NECO).

**Cherry Greiner** is a senior biomedical engineer at Infraredx, a spectroscopy- and IVUS-based intravascular imaging company. She received her BEng degree in engineering physics from McMaster University. With research interests in biomedical optics, she pursued her PhD in biomedical engineering from Tufts University, developing a light scattering-based flow cytometry for cancer cell enumeration. She continued her research interests as a postdoctoral fellow at NECO, where she initiated the development of the AO-SLO-OCT system.

**John S. Werner** is a distinguished professor of ophthalmology and neurobiology at the University of California, Davis. His research is focused on retinal structure and function in normal aging and disease. He received his PhD from Brown University, and was previously a professor at the University of Colorado, Boulder.

**Nathan Doble** is an associate professor in the College of Optometry and also in the Department of Ophthalmology and Visual Science at OSU. His research interest is the development of high-resolution optical imaging systems for the visualization of the human retina. He holds his MSci, MSc, and PhD degrees in the fields of laser physics and adaptive optics and performed postdoctoral work at the University of Rochester, New York, USA. He was a cofounder of Iris AO Inc. before joining OSU.